surfaces

MDPI

Article

The Work Function of TiO_2

Shun Kashiwaya [1,2], Jan Morasch [1], Verena Streibel [1,†], Thierry Toupance [2], Wolfram Jaegermann [1] and Andreas Klein [1,*]

[1] Department of Materials and Earth Sciences, Surface Science Division, Technische Universität Darmstadt, Otto-Berndt-Straße 3, 64287 Darmstadt, Germany; skashi@surface.tu-darmstadt.de (S.K.); j.morasch@web.de (J.M.); streibel@stanford.edu (V.S.); jaegerw@surface.tu-darmstadt.de (W.J.)

[2] Institute of Molecular Sciences, University of Bordeaux, CNRS UMR 5255, Bâtiment A12, 351 Cours de la Liberation, 33405 Talence CEDEX, France; thierry.toupance@u-bordeaux.fr

* Correspondence: aklein@surface.tu-darmstadt.de; Tel.: +49-6151-16-20772

† Current address: SUNCAT Center for Interface Science and Catalysis, SLAC National Accelerator Laboratory, 2575 Sand Hill Road, Menlo Park, CA 94025, USA.

Received: 13 July 2018; Accepted: 1 September 2018; Published: 7 September 2018

Abstract: Polycrystalline anatase thin films, (001)- and (101)-oriented anatase TiO_2 single crystals and (001)- and (110)-oriented rutile TiO_2 single crystals with various surface treatments were studied by photoelectron spectroscopy to obtain their surface potentials. Regardless of orientations and polymorph, a huge variation of the Fermi level and work function was achieved by varying the surface condition. The most strongly oxidized surfaces are obtained after oxygen plasma treatment with a Fermi level ∼2.6 eV above the valence band maximum and ionization potentials of up to 9.5 eV (work function 7.9 eV). All other treated anatase surfaces exhibit an ionization potential independent of surface condition of 7.96 ± 0.15 eV. The Fermi level positions and the work functions vary by up to 1 eV. The ionization potential of rutile is ∼0.56 eV lower than that of anatase in good agreement with recent band alignment studies.

Keywords: TiO_2; anatase; rutile; work function; electron spectroscopy; photocatalysis

1. Introduction

Titanium dioxide (TiO_2) is widely applied in photocatalysis [1] and as electrode in solar cells [2], and has been considered to be a promising material owing to its physical and chemical properties. Among the different polymorphs of TiO_2, mostly fundamental properties of rutile have been studied experimentally and theoretically despite a superior photocatalytic activity of anatase as compared to rutile, which is associated with its longer charge carrier life time and higher carrier mobility [3]. Oriented rutile substrates, of which the rutile (110) is the most stable and can be easily prepared, have been thoroughly investigated as model surfaces for fundamental surface phenomena [4]. In contrast, information about oriented anatase is sparse because of their difficult preparation [5]. Only recently novel techniques to prepare oriented anatase substrates have been developed [6]. In 2008 Yang et al. [7] synthesized anatase single crystals with 47% of the minority (001) facet via a hydrothermal route employing fluoric acid. This successful synthesis has surged further fundamental investigations of both anatase (101) and (001) facets [8–11]. However, although the electronic structure of anatase bulk and surfaces including band gaps and surface states are well known due a wide range of experimental and theoretical studies using complementary techniques, particularly using electron spectroscopy (see e.g., [11–21]), the surface potentials—Fermi level position, work function and ionization potential—have not yet been studied systematically.

The work function φ of materials is especially relevant for photocatalysis and solar cells as it governs the band alignments of interfaces such as TiO_2/metal contacts forming Schottky barriers,

TiO_2/p-type semiconductor interfaces forming p-n junctions, and TiO_2/liquid junctions related to redox potentials. Despite its importance for TiO_2, only few work function data have been reported [22–24]. The work function is affected by the Fermi energy E_F and by the vacuum energy E_{vac}, which can be manipulated separately by doping, surface space charge layers, or the surface dipole, respectively [25]. The latter depends on surface polarity and termination [26]. Changes in the surface dipole directly affect the ionization potential I_P, which is the difference between vacuum energy and valence band maximum E_{VB} and which does not depend on the Fermi energy.

The ionization potential of metal oxide surfaces depends on surface orientation and surface termination, where the latter can vary with the oxygen activity during preparation [25,27–31]. Due to a strong electronegativity of oxygen, less oxygen results in a lower negative surface charge and thus in a lower I_P and φ. The oxygen activity also affects the Fermi energy in oxides. A lower oxygen activity, i.e., more reducing conditions, generally results in a higher Fermi energy and thereby in a lower $\varphi = E_{vac} - E_F$. Detailed data on the interplay between the surface potentials and oxygen activity for most TiO_2 surfaces are still lacking.

Figure 1 displays a ball-and-stick model of bulk-terminated surfaces of rutile (110) and (001), and anatase (101) and (001) without structural relaxations. At the rutile (110) surface bridging oxygen atoms missing one bond to Ti can be easily removed by thermal annealing, whereas at the rutile (001) surface, oxygen vacancies V_O are believed to easily form at a twofold-coordinated surface O atom [4,32]. It was theoretically predicted and experimentally shown that the point defect is located at the bridging oxygen row on the rutile (110) surface whereas for the anatase (101) surface V_O are favored to be situated in the subsurface rather than on the surface [18,33–35]. At anatase (101) and (001) surfaces, the V_O has a lower formation energy in the subsurface than on the surface while the rutile (110) surface exhibits an inverse trend. Thus, at anatase (101) and (001) surfaces, V_O are energetically stable in the subsurface or even in the bulk whereas at rutile (110) and (001) surfaces, the V_O form most likely at the bridging oxygen site on the top surface. This difference in oxygen vacancy distribution is expected to lead to different electronic properties.

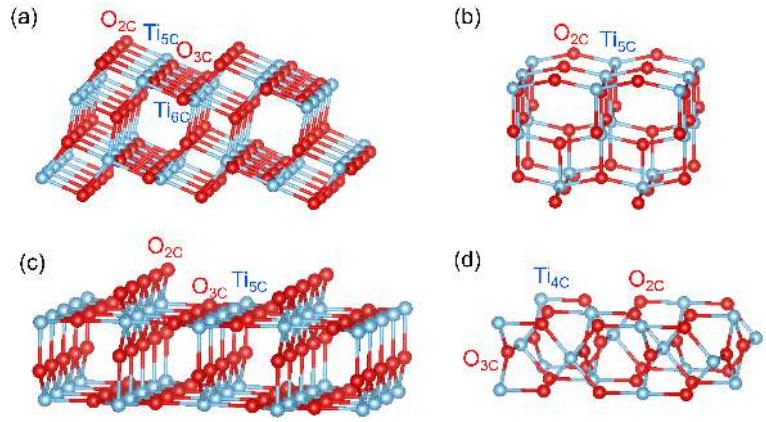

Figure 1. Bulk-terminated surfaces of (**a**) anatase (101), (**b**) anatase (001), (**c**) rutile (110) and (**d**) rutile (001), illustrated using VESTA.

Many applications of TiO_2 such as water splitting, water purification and self-cleaning, undergo an interaction with water [36–39]. Thus, the investigation of water adsorption on the surface is important. Water adsorption has therefore been investigated intensively by many groups with different techniques (see e.g., [4,40–50] and references therein). Studies of water adsorption on TiO_2 are usually performed at liquid nitrogen or lower temperature, where multilayers of molecular water can be adsorbed in a vacuum system [51]. Many studies have focused on the initial state of adsorption: molecular, dissociative, or multilayer adsorption. Most calculations have predicted that on rutile (110) surfaces dissociative adsorption of water is energetically preferred over molecular adsorption [4]. However,

there is a consensus established by several experiments that water dissociates only at the vacancy sites of so-called bridging oxygen rows while only molecular adsorption takes place on the stoichiometric defect-free rutile (110) surface [4,40,41]. For anatase, it was found that water adsorbs dissociatively on the surface in the presence of subsurface V_O, although it has also been reported that water would adsorb only molecularly on the anatase surfaces [42–46]. Based on these reports, we assume that the distribution of V_O influences the interface of TiO_2 and water, which affects photocatalytic redox reactions. Despite the wealth of studies on this subject, it remains largely unknown how water adsorption affects the work function of different surfaces.

In this work, (001)- and (101)-oriented and polycrystalline anatase surfaces in different oxidation conditions were studied. The same treatments were applied to rutile (110)- and (001)-oriented surfaces. Polycrystalline anatase thin films prepared by spray pyrolysis are also included in this study. The chemical and electronic surface properties were accessed using X-ray und UV photoelectron spectroscopy (XPS and UPS). The reported results provide the variation of the surface potentials of TiO_2, i.e., the Fermi level position (E_F) with respect to the valence band maximum (E_{VB}) and the work function φ, with surface condition. For anatase, we have also studied the variation of surface properties after exposure to water vapor at room temperature without breaking vacuum. Furthermore, we compare anatase and rutile surfaces and discuss differences in their electronic properties. Overall, the work provides guidance towards manipulating the work function of TiO_2 surfaces.

2. Materials and Methods

Natural anatase crystals were employed for both (101) and (001) surfaces (SurfaceNet GmbH, Rheine, Germany). Polycrystalline anatase substrates were prepared by spray pyrolysis. Epitaxially polished rutile (110) and (001) substrates were purchased from CrysTec GmbH (Berlin, Germany). The size of the substrates is $5 \times 5 \times 1$ mm^3. A surface roughness less than a lattice constant was achieved after epi-polishing the single crystal substrates. For anatase, in addition to the ex-situ surfaces (ex-a(001), ex-a(101), and ex-a-poly) with contamination from air and polishing, unreconstructed (101) and (001), and polycrystalline surfaces were in situ prepared inside an integrated vacuum system to expose different well-defined stoichiometries: sputtered (sp-a(001), sp-a(101), and sp-a-poly), annealed (an-a(001), an-a(101), and an-a-poly), oxidized (ox-a(001), ox-a(101), and ox-a-poly), and stoichiometric (st-a(001), st-a(101), and st-a-poly). For rutile, annealed (an-r(110) and an-r(001)) and oxidized (ox-r(110) and ox-r(001)) were prepared.

Sample preparations and measurements were carried out in the Darmstadt integrated system for materials research (Daisy-Mat) [52] equipped with a multitechnique surface analysis system Physical Electronics PHI 5700, which is connected to different sample preparation chambers via a sample transfer system. The sputtered surfaces were prepared by repeated cycles of Ar^+ ion sputtering with an energy of 1 keV for 15 min and annealing under ultrahigh vacuum (UHV) conditions at 873 K for 30 min until no remaining emissions from contaminations were observed by X-ray photoelectron spectroscopy (XPS). Although this procedure has been conventionally accepted to prepare clean surfaces of single crystal TiO_2, Ar sputtering not only results in a highly reduced surface and thus leads to the formation of oxygen vacancies and Ti^{3+} surface states, but also partially destroys the crystallinity of the surface and introduces an amorphous phase [4,6,53].

After Ar ion etching, the sputtered surfaces were oxidized in an Oxygen plasma at room temperature in an atmosphere of 7.5×10^{-5} mbar O_2 for 15 min to re-oxidize the surface, followed by annealing at 873 K in UHV to re-crystallize the surface. Here the O plasma was selected to replenish the lattice O instead of annealing in O_2 atmosphere, which has been frequently used for oxidation, as annealing in O_2 could form additional incomplete reconstructions [54]. Furthermore, annealing in O_2 may lead to iron oxide layer formation since elevated temperatures may trigger the surface segregation of Fe, which is a typical contamination of natural anatase crystals [6]. In addition, atomic O in the O plasma is more oxidative than molecular O_2 during annealing in O_2 atmosphere, which leads to partially remaining V_O [18,55].

The surfaces, which are in this work referred to as *annealed*, (The term *annealing* might be used differently in literature) were prepared by an oxygen plasma treatment and a subsequent reduction by annealing in vacuum at 873 K. Low energy electron diffraction (LEED) patterns recorded for these surfaces are shown in Figure A1. They show unreconstructed 1×1 patterns with low background intensity, indicating well-ordered surfaces. Finally, the stoichiometric surfaces were prepared by removing O adatoms by annealing the oxidized (plasma treated) surfaces in UHV at 473 K for 20 min [56,57]. An overview of the preparation procedures for the above described different surfaces is given in Figure 2. It is noted that the color of rutile substrates, which are less conductive than anatase, changed from transparent into dark blue after the reduction procedure, making the surfaces sufficiently conductive to avoid charging during photoemission measurements.

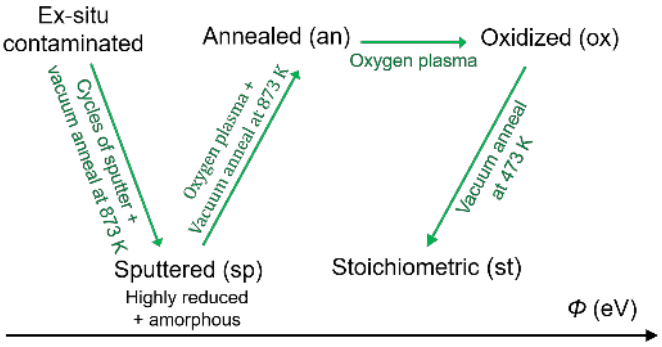

Figure 2. Scheme of the preparation procedure for ex-situ (ex), sputtered (sp), annealed (an), oxidized (ox), and stoichiometric (st) surfaces of the TiO_2 surfaces.

To further understand the electronic structures of different surfaces in a practical situation for photocatalytic reactions, water was dosed through a diaphragm valve for atomic layer deposition in a vacuum chamber [58] onto the annealed, oxidized, and stoichiometric surfaces for the anatase (001) and (101), and polycrystalline anatase. The water exposure at room temperature was completed using 15 water pulses of 0.5 s duration followed by evacuation for 60 s. The amount of exposed water molecules in this process depends on the pumping speed and the chamber geometry. We estimate the exposure to 10^6–10^8 Langmuir. The resulting TiO_2 substrates were transferred to the XPS chamber and investigated immediately after this adsorption procedure. XPS analysis revealed a small C 1s emission after water exposure.

X-ray photoelectron spectra were recorded with monochromatic Al Kα radiation at an emission angle of 45° and a pass energy of 5.85 eV, which gives a total energy resolution of 0.4 eV, as determined from the Gaussian broadening of the Fermi edge of a sputter-cleaned Ag sample. Binding energies of core levels and the valence band maximum E_{VB} can be determined with an accuracy of 50 meV, and 100 meV, respectively. For the determination of work function φ and ionization potentials I_P, ultraviolet photoelectron spectra were recorded in normal emission with He I radiation ($h\nu = 21.2$ eV) from a He discharge lamp and a negative sample bias of 4.0 V. The total energy resolution is 0.2 eV. No charging problems were observed during the XPS and UPS measurements. Obtained binding energies for XPS and UPS were calibrated by the Fermi level energy of a sputter-cleaned Ag sample. Hence, all binding energies are given with respect to the calibrated Fermi level at 0 eV. More details of the experimental setup and approach in performing the experiments may be found elsewhere [52,59].

3. Results and Discussion

The Ti $2p_{3/2}$ and O 1s core level spectra of the differently treated surfaces are shown in Figure 3. The Ti $2p_{3/2}$ emission of the sputtered anatase (101) surface shows a strong low binding energy emission associated with Ti^{3+} and Ti^{2+} shifted relative to the main emission line of Ti^{4+} by ~1.7 and ~3.5 eV, respectively [45,60,61]. All other samples, including the sputtered anatase (001), exhibit sharp

and symmetric lines consisting of a single Ti^{4+} oxidation state. Evidently, the anatase (101) surface is much easier reduced than the (001) surface. The low binding energy Ti $2p_{3/2}$ emissions related to surface reduction of anatase (101) are neither observed after re-oxidation by O plasma treatment nor after re-crystallization by annealing in vacuum.

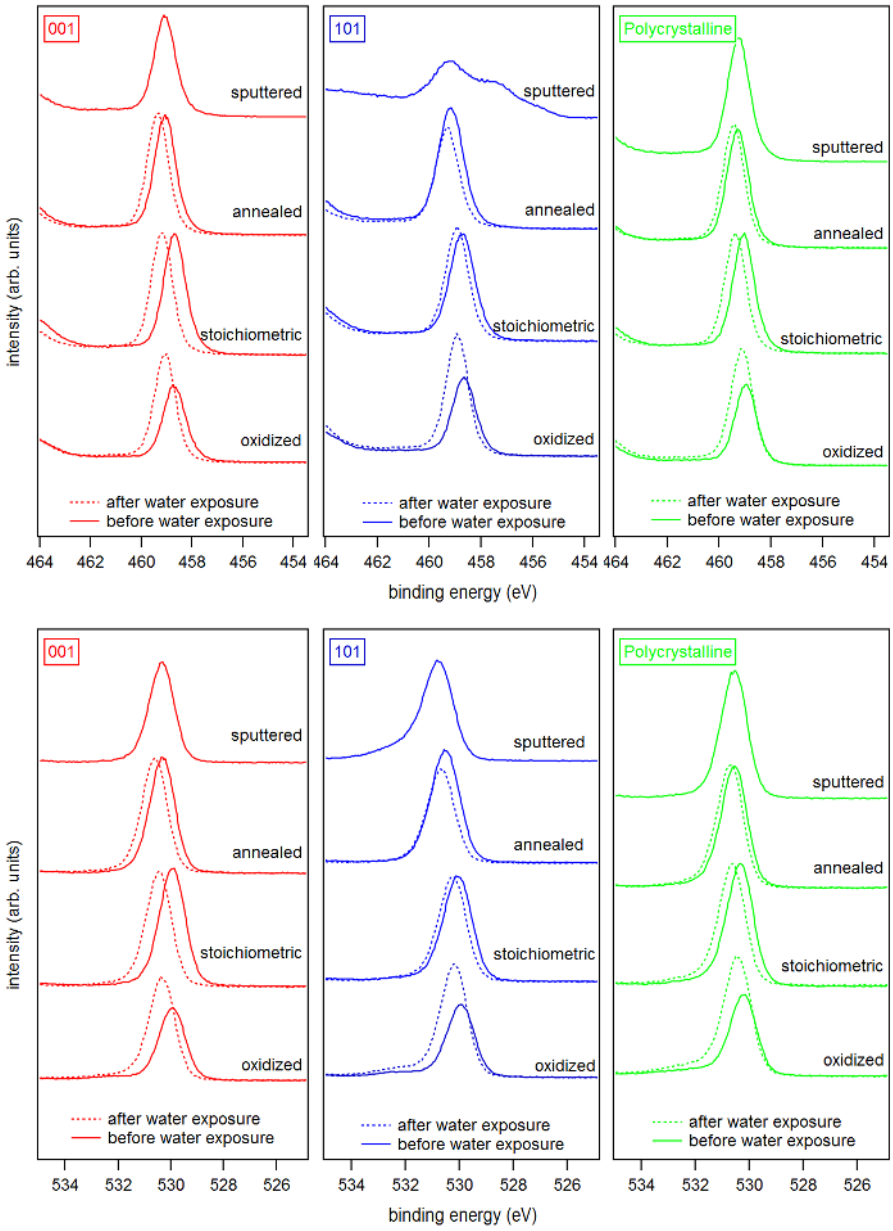

Figure 3. X-ray photoelectron spectra of the Ti $2p_{3/2}$ (**top**) and the O 1s (**bottom**) core level emissions of (**left**) anatase (001), (**middle**) anatase (101), and (**right**) polycrystalline anatase substrates with sputtered, annealed, stoichiometric, and oxidized surfaces. Solid and dash lines represent spectra before and after water exposure, respectively.

Exposing an-a(001) and an-a(101) to an O plasma results in a shoulder in the O 1s emission at 3 eV higher binding energy compared to the O 1s emission related to TiO_2 (see bottom row of Figure 3). This shoulder is likely attributed to peroxo (O_2^{2-}) surface species, like for example in bridging oxygen dimers [62]. The stoichiometric anatase (001) and (101) surfaces show no shoulder in the O 1s emission

after annealing in vacuum at 473 K. The surface peroxo species observed after oxygen plasma treatment at ox-a(001) and ox-a(101) is therefore effectively removed by annealing.

X-ray and ultraviolet valence band spectra are shown in Figure 4. UP spectra are usually more sensitive to surface defects than XP spectra, which is mostly due to the higher surface sensitivity of UPS and the higher intensities. It is accepted that the so-called band gap surface states would form due to occupied Ti 3d states (Ti^{3+}) near the O vacancy sites on the surface, but also due to Ti^{3+} interstitials in the subsurface region [4,11,18,63,64]. It is clear from Figure 4 that all sputtered TiO_2 surfaces show the well-known Ti $3d^1$ emission lines in the band gap region.

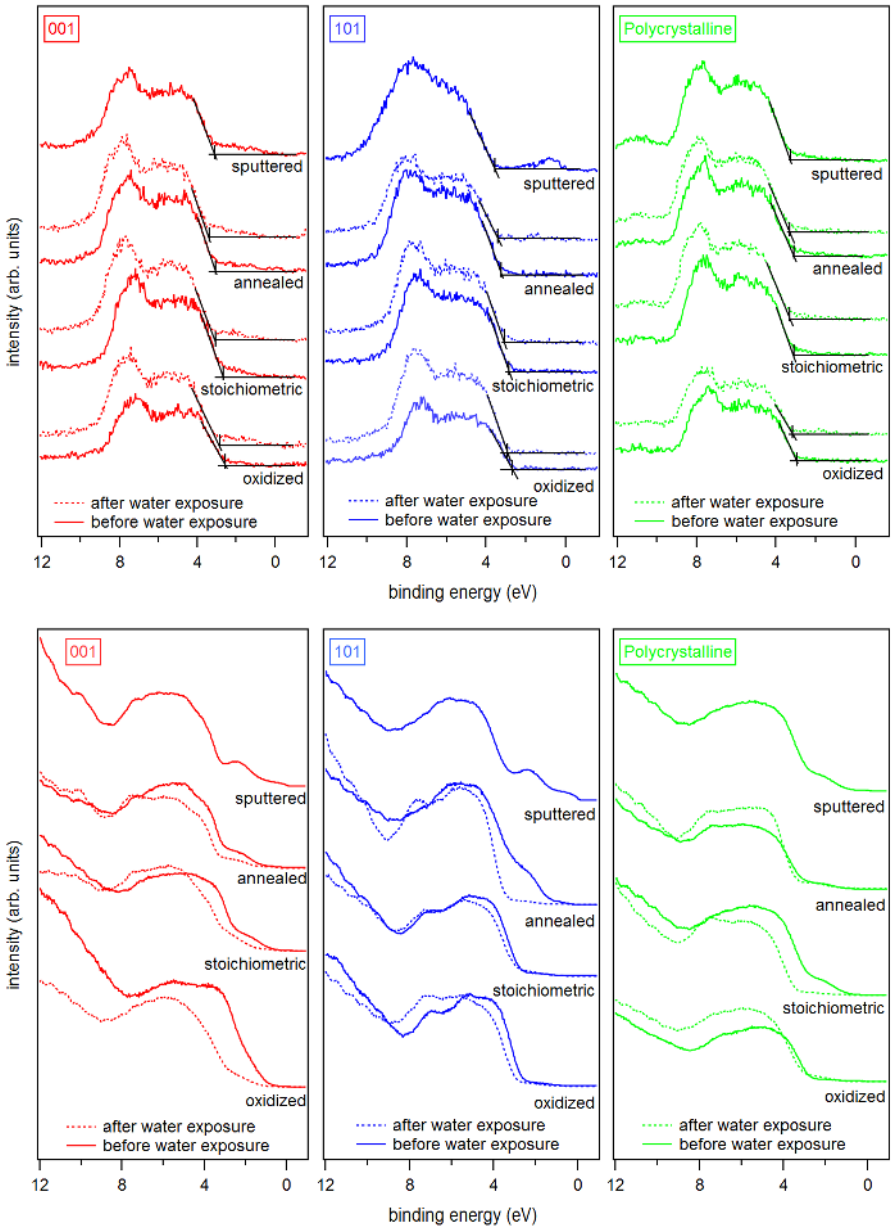

Figure 4. X-ray (**top**) and ultraviolet (**bottom**) valence band spectra of sputtered, annealed, stoichiometric, and oxidized surfaces for (**left**) anatase (001), (**middle**) anatase (101), and (**right**) polycrystalline anatase substrates before and after water exposure.

The emission of the gap states is different for the (001) and (101) surface orientation of anatase. The state energically closer to the Fermi energy at a binding energy of ~0.5 eV is more pronounced for

the (101) surface. As this emission is clearly observed only for the sputtered (101) surface, this shallow gap state is likely related to the observation of the reduced Ti species.

The intensity of the band gap states is generally reduced with surface oxidation for both orientations and all treatments. However, the deep gap state, which is closer to the onset of the valence band maximum at 1.5–2.0 eV binding energy, is still observed in the XP and the UP valence spectra for the (001) surface even after O plasma treatment. In contrast, the deep gap state is completely attenuated for the oxidized and the stoichiometric (101) surface.

The valence band maximum binding energies $E_F - E_{VB}$ are determined by a linear extrapolation of the low binding energy valence band emission edge. Only XPS data are used here as they are less affected by the gap state emissions. The extracted values are summarized in Table 1 together with the core level binding energies, which are determined from the spectra shown in Figure 3.

Table 1. Binding energies (Ti 2p and O 1s), Fermi level position $E_F - E_{VB}$, work function φ, and ionization potential I_P for anatase (001), anatase (101), and polycrystalline anatase, as well as for rutile (001) and rutile (110) with different surface stoichiometries: sputtered, annealed, stoichiometric, oxidized and ex-situ prepared surfaces. Number in brackets are obtained after in situ exposure to water vapor at room temperature.

	Sputtered	**Annealed**	**Stoichiometric**	**Oxidized**	**Ex-Situ**
			Ti $2p_{3/2}$ (eV)		
a-(001)	459.08	459.07 (459.36)	458.70 (459.20)	458.64 (459.06)	459.27
a-(101)	459.21	459.17 (459.31)	458.73 (458.93)	458.69 (458.91)	459.28
a-poly	459.25	459.28 (459.44)	459.06 (459.37)	458.95 (459.09)	
r-(001)		459.38		458.78	
r-(110)		459.35		458.95	
			O 1s (eV)		
a-(001)	530.35	530.33 (530.62)	529.95 (530.47)	529.93 (530.32)	530.60
a-(101)	530.81	530.52 (530.68)	530.07 (530.27)	529.93 (530.19)	530.62
a-poly	530.57	530.56 (530.71)	530.35 (530.64)	530.20 (530.44)	
r-(001)		530.69		530.04	
r-(110)		530.62		530.21	
			$E_F - E_{VB}$ (eV)		
a-(001)	3.10	3.06 (3.39)	2.64 (3.06)	2.53 (2.87)	3.44
a-(101)	3.55	3.23 (3.40)	2.84 (3.08)	2.69 (2.91)	3.35
a-poly	3.23	3.09 (3.37)	3.12 (3.31)	2.94 (3.16)	
r-(001)		3.07		2.57	
r-(110)		3.12		2.68	
			φ in (eV)		
a-(001)	4.70	4.72 (4.36)	5.35 (4.34)	6.44 (4.97)	3.61
a-(101)	4.62	4.72 (4.36)	5.23 (4.40)	6.76 (5.03)	3.65
a-poly	4.51	4.23 (4.22)	5.16 (4.38)	5.62 (4.94)	
r-(001)		4.29		6.08	
r-(110)		4.31		5.96	
			I_P (eV)		
a-(001)	7.80	7.78 (7.75)	7.99 (7.40)	8.97 (7.84)	7.05
a-(101)	8.17	7.95 (7.76)	8.07 (7.48)	9.45 (7.94)	7.00
a-poly	7.74	7.32 (7.59)	8.28 (7.69)	8.56 (8.10)	
r-(001)		7.36		8.65	
r-(110)		7.43		8.64	

Independent of surface orientations, the valence band maximum binding energy decreases in the order sputtered, annealed, stoichiometric, and oxidized treatment. The valence band maximum and the core levels show comparable binding energy shifts. In particular, the binding energy difference between the O 1s and the Ti 2p core level is 71.29 ± 0.04 eV, with the only exception of the sputtered anatase surface, where the binding energy of the Ti 2p core level is more uncertain due to the strong

reduction of the surface. The binding energy differences between the core levels and valence band maxima also remain within ±0.15 eV, which can also be considered to be constant considering the changes of the valence bands in dependence on treatment. The binding energy shifts can therefore be attributed to different Fermi energies. These are likely caused by different concentrations of oxygen vacancies at the surface or in the bulk. The former would cause binding energy shifts due to surface electron accumulation, the latter due to enhanced doping.

The overall variation of the Fermi energy is 0.46 eV for the (001) and 0.71 eV for the (101) surface orientation, respectively. It is noteworthy that $E_F - E_{VB}$ of the (101) surface is always higher than that of the (001) surface. This difference of $E_F - E_{VB}$ results in a variation of surface potential with orientation, which will drive photogenerated electrons and holes towards the (101) and (001) surfaces, respectively. This charge separation mechanism agrees with literature reports [65,66].

The secondary electron edges of the UP spectra of anatase are shown in Figure 5. Their energetic position is determined at the middle of the steep rise of the edge. (Most authors use the intersection of the secondary electron edge with the baseline to determine the work function. We take the middle of the steep rise instead as we assume that the onset is broadened by the resolution of the spectrometer system. We use this procedure when the width of the steep part of the edge is ≤0.2 eV, which is the case for all spectra in this manuscript. In this case, the difference between the two approaches is less than 0.1 eV.) The extracted work functions φ and ionization potentials I_P are summarized in Table 1 and the work function is plotted as a function of the Fermi energy in Figure 6. More extended data including polycrystalline and water exposed samples are provided in the appendix in Figure A2 and Table A1. The work functions are decreasing in the order oxidized > stoichiometric > annealed > sputtered for both single crystal anatase surface orientations. It therefore decreases monotonically with the increase of the Fermi level to valence band maximum distance, $E_F - E_{VB}$. This is to be expected as both depend on the oxidation state of the surface and subsurface. Similar dependencies have been reported for ZnO, In_2O_3 and SnO_2 [25].

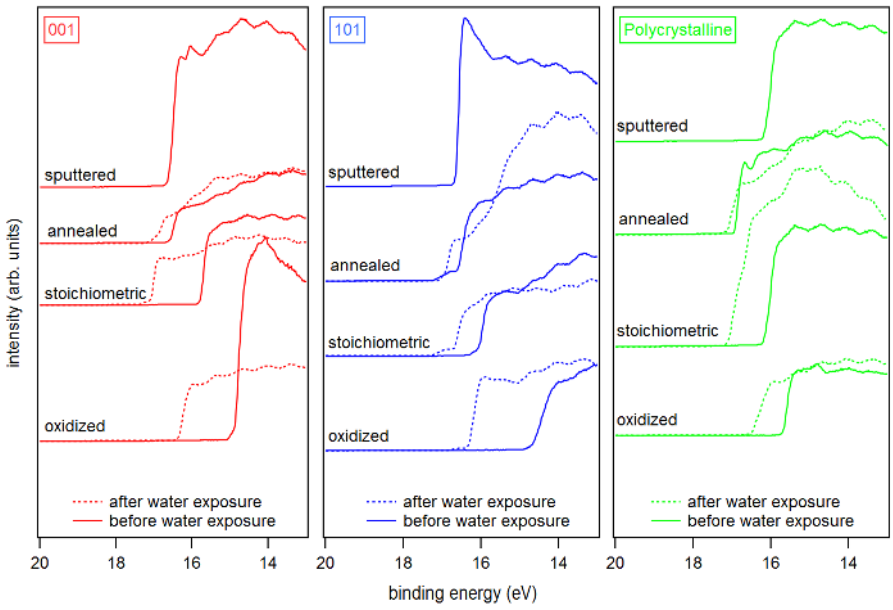

Figure 5. UP spectra of SEE of sputtered, annealed, stoichiometric, and oxidized surfaces for anatase (001), anatase (101), and polycrystalline anatase substrates before and after water exposure.

The overall variation of the work function is 1.74, 2.14 and 1.39 eV for anatase (001), anatase (101) and polycrystalline anatase, respectively. The change of φ between stoichiometric, annealed, and sputtered single crystal surfaces is caused mainly by a change of $E_F - E_{VB}$ as the ionization potential is almost constant for these surface conditions with $I_P = 7.96 \pm 0.15$ eV. Such a behavior has also been

reported by Henrich et al. for rutile (110) surfaces [22]. The ionization potential of the polycrystalline surfaces varies more with preparation conditions than at the single crystalline surfaces. This is likely attributed to a less pure surface condition, as the surfaces typically show residual carbon contamination. Considerably higher ionization potentials of up to 9.45 eV are observed for the oxygen plasma treated surfaces. This matches with the assumed peroxo or bridging oxygen species on the surface, which are induced by radical oxygen atoms of the oxygen plasma. Electronegative oxygen accumulates with a negative charge, leading to high work functions and ionization potentials of oxidized surfaces due to an increase of the surface dipole [31,67].

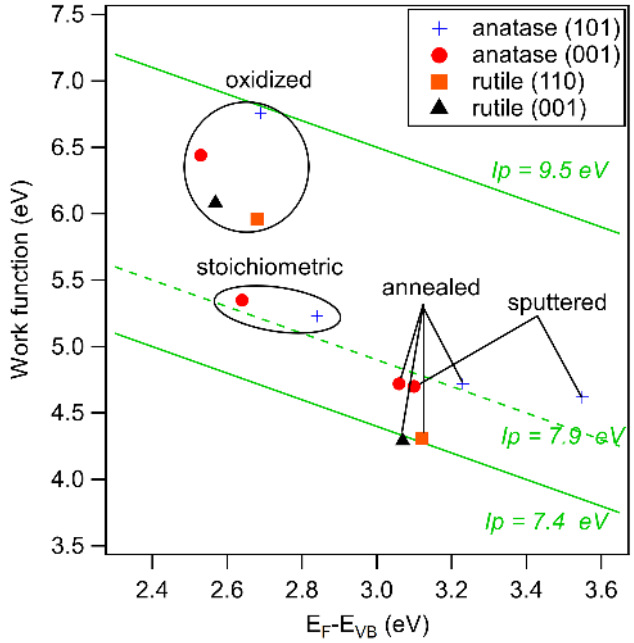

Figure 6. Work function versus Fermi level to valence band maximum distance, $E_F - E_{VB}$, of sputtered, annealed, stoichiometric, and oxidized surfaces for anatase (001), anatase (101), and polycrystalline anatase substrates before and after water exposure. Values for annealed and oxidized rutile (001) and (110) surfaces are added for comparison.

Water vapor was exposed to the surfaces at room temperature and the resulting electronic properties were investigated by XPS and UPS. Obtained core level binding energies and surface potentials of the surfaces exposed to water are included in brackets in Table 1. The chemical modification of the surface resulting from water exposure is not clear. During low temperature adsorption, a mixture of molecular and dissociative adsorption is reported [4,40–46]. The adsorption of water molecules is not expected at room temperature in ultra-high vacuum but formation of hydroxides is likely. However, we do not have a clear confirmation for this. The O 1s peaks do not show the high binding energy shoulder typical for hydroxides. Nevertheless, the O 1s spectra do exclude a low OH coverage. Further studies, which are beyond the scope of the present work, are required to resolve the interaction of water vapor with TiO_2 surfaces.

Irrespective of the uncertainty of the chemical state of the surface, water exposure reproducibly induces shifts of the Ti 2p and O 1s core levels and the valence band edge towards higher binding energies. The shifts can therefore be attributed to a downward band bending at the TiO_2 surface, resulting in an accumulation of electrons at the surface. This observation emphasizes the importance of adsorbates for the frequently reported electron accumulation layers at oxide surfaces [68–70]. The final Fermi level positions, which are extracted from the valence band maximum and the core level binding energies do not depend on surface orientation and are ∼3.4, ∼3.1 and ∼2.9 eV for the annealed, stoichiometric and oxidized (001) and (101) surfaces, respectively. The original difference in $E_F - E_{VB}$

between the anatase (101) and (001), which was present for all surface conditions, thus disappeared after water exposure.

The work function after water exposure is ∼4.4 eV for the annealed and stoichiometric surfaces, while it is significantly higher (∼5.0 eV) for the oxidized surface. Apparently, the adsorbed peroxo or bridging oxygen species, which cause the increased ionization potential, are not completely removed by water exposure. These species are therefore strongly enough bound to the surface to withstand the reduction of the sample by water exposure. The latter is indicated by the rise of the Fermi energy.

XP spectra of the valence band region, the Ti $2p_{3/2}$, and the O 1s core levels of annealed and oxidized rutile (001) and (110) surfaces are shown in Figure 7. Corresponding core level binding energies and surface potentials are included in Table 1. Obtained work functions and ionization potentials are plotted together with the anatase data in Figure 6. A large difference of $E_F - E_{VB}$ and φ between the two treatments but no significant dependence on surface orientation are observed. The ionization potential of the annealed surfaces amounts to 7.40 ± 0.04 eV, which is 0.56 eV lower than that of the corresponding anatase surfaces.

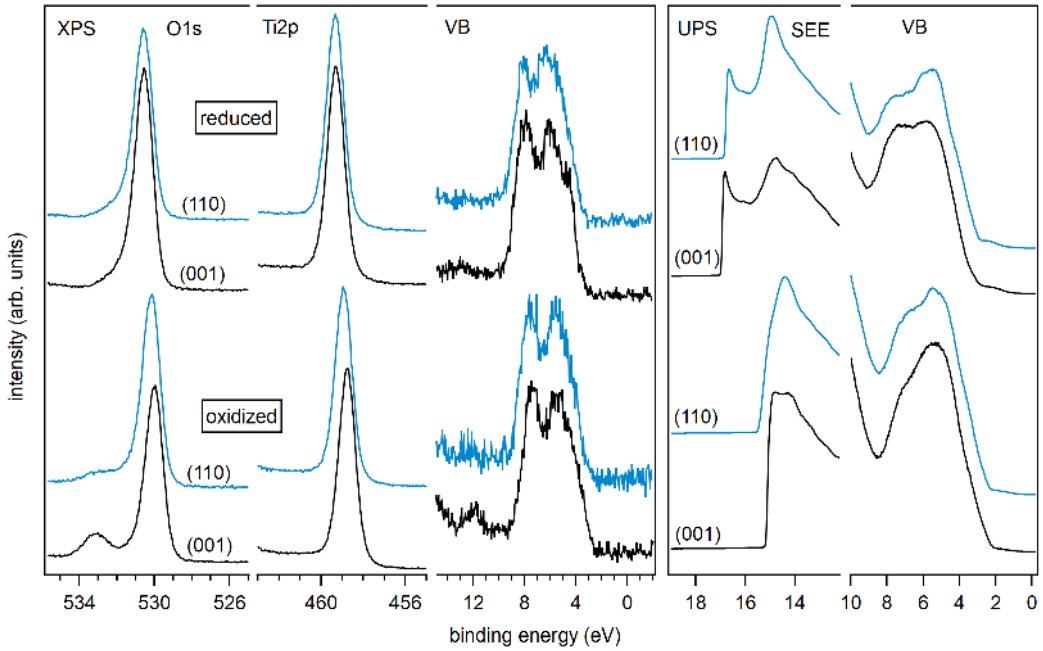

Figure 7. XP spectra of Ti 2p, O 1s, and valence band emission lines, and UP spectra of secondary electron edge and valence band region for rutile (001) and (110) substrates with reduced and oxidized surfaces.

The ionization potentials of the anatase and rutile surfaces (except for the ones treated in the O plasma), which are 7.96 and 7.40 eV, respectively, are comparable to those of ZnO surfaces exposed to oxidizing conditions (∼7.6 eV) [25,29]. Similar ionization potentials are also found for surfaces of Sn-doped In_2O_3 (∼7.7 eV) and reduced SnO_2 surfaces [25,29,71,72]. The latter are characterized by a Sn^{2+} oxidation state [28,73–75]. Except for the sputtered anatase (101) surfaces, which exhibits substantial reduction of Ti, most of the Ti adopts a +IV oxidation state. One might therefore expect that the ionization potential is comparable to that of the stoichiometric SnO_2 surface, which amounts to ∼8.9 eV [25,29,71,72]. The deviation is quite substantial, even for rutile, which has the same crystal structure as SnO_2. The ionization potential of TiO_2 is therefore substantially lower than that of SnO_2. TiO_2 surfaces do also not show the variation of cation oxidation state and the associate change of I_P, which is characteristic for SnO_2. The origin of these remarkable differences remains to be resolved. Due to the similar ionization potentials and work functions of TiO_2, ZnO and In_2O_3, the superior

photocatalytic and solar cell properties of TiO_2 are probably not caused by an advantageous energy band alignment.

The difference in ionization potential between anatase and rutile amounts to ∼0.5 eV. Aligning the vacuum energies of the two polytypes does therefore result in a valence band maximum of anatase being ∼0.5 eV lower in energy than that of rutile. This is the same direction and of the same magnitude as the energy band alignment established recently by different experimental and theoretical approaches [19,76,77], supporting the conclusion that the energy bands of rutile are higher than those of anatase.

4. Summary and Conclusions

Chemical and electronic properties of anatase (001), anatase (101), polycrystalline anatase, rutile (110) and rutile (001) with different surface treatments were studied using XPS and UPS. The Fermi energy and work function depend drastically on surface conditions, which are characterized by different oxygen vacancy concentrations and surface adsorbates. We have shown how the surface Fermi energy, work function and ionization potentials are affected and can therefore be adjusted by different surface treatments.

For anatase, the Fermi level can be manipulated between $E_F - E_{VB} = 2.53$–3.10, 2.69–3.55, and 2.94–3.23 eV for the (001), (101) and polycrystalline surfaces, respectively. Along with the different Fermi energies goes a variation of work function between $\varphi = 4.70$–6.44, 4.62–6.76, and 4.51–5.62 eV for the (001), (101) and polycrystalline surfaces, respectively. Apart from the plasma treated samples, which have exceptionally high work functions likely due to the presence of peroxo species, the ionization potential is rather insensitive to the surface treatments and exhibits a value of $I_P = 7.96 \pm 0.15$ eV. This is approximately 0.5 eV higher than of rutile, which agrees with the band alignment obtained from other techniques. For the anatase samples, the Fermi energy at the (101) surface is furthermore higher than at the (001) surface for all surface treatments.

Exposure of the samples to water vapor at room temperature reproducibly causes a downward band bending on all surfaces (rise of the Fermi energy). For the anatase surfaces, the dependence of Fermi energy on surface orientation is removed by water exposure. Water exposure also affects the ionization potential. Together, both effects result in a lowering of the work function down to 4.34 ± 0.06 eV ($I_P = 7.61 \pm 0.15$ eV) for the annealed and the stoichimetric surfaces. The ionization potential of the plasma treated surfaces remains rather high (7.96 ± 0.13 eV), resulting in work functions of 4.98 ± 0.05 eV after water exposure.

Author Contributions: Single and polycrystalline surfaces were prepared and analyzed by S.K. and J.M., supervised by A.K., W.J. and T.T.; Discussion and interpretation of results was conducted by S.K., A.K. and W.J.; The original draft has been composed by S.K., edited by A.K. and revised by all authors; Funding has been acquired by W.J. and T.T.

Funding: This work was partly supported by the European Commission within the Erasmus Mundus Joint Doctoral program International Doctoral School in Functional Materials for Energy, Information Technology, and Health (ids-funmat), the French-German University (UFA Doctoral College in Functional Materials for Energy and Information Technology) and was carried out within the framework of EMMI (European Multifunctional Material Institute). Further support was received from the European Commission under the FP7 project "Novel Composite Oxides by Combinatorial Material Synthesis for Next Generation All-Oxide-Photovoltaics," project number 309018.

Acknowledgments: Receipt of polycrystalline samples from Arie Zaban's group at Bar Ilan University, Israel, is also gratefully acknowledged.

Conflicts of Interest: The authors declare no conflict of interest. The founding sponsors had no role in the design of the study; in the collection, analyses, or interpretation of data; in the writing of the manuscript, and in the decision to publish the results.

Abbreviations

The following abbreviations are used in this manuscript:

XPS	X-ray photoelectron spectroscopy
UPS	ultraviolet photoelectron spectroscopy
UHV	ultra-high vacuum
LEED	low-energy electron diffraction

Appendix A. LEED Pattern for Annealed Anatase Surfaces

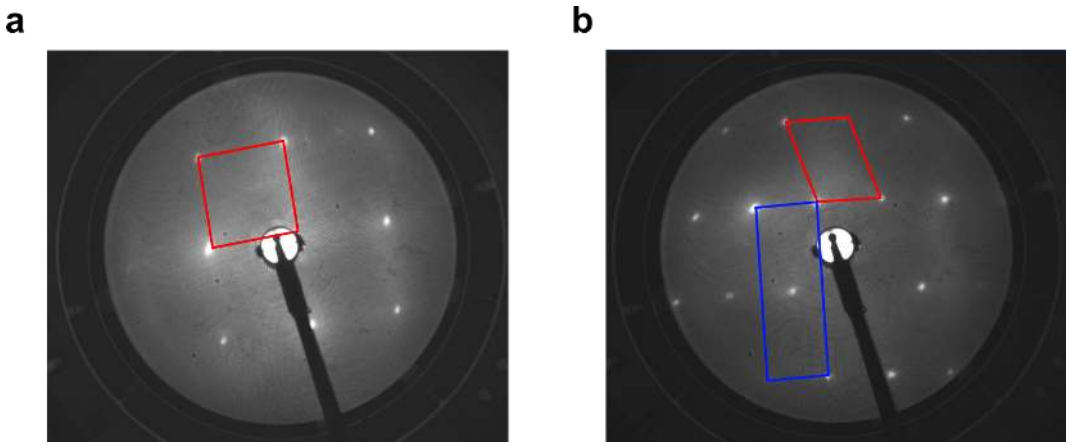

Figure A1. LEED pattern of the annealed anatase (001) (**a**) and (101) (**b**) surfaces. The unit cells are indicated.

Appendix B. Further Work Function Data

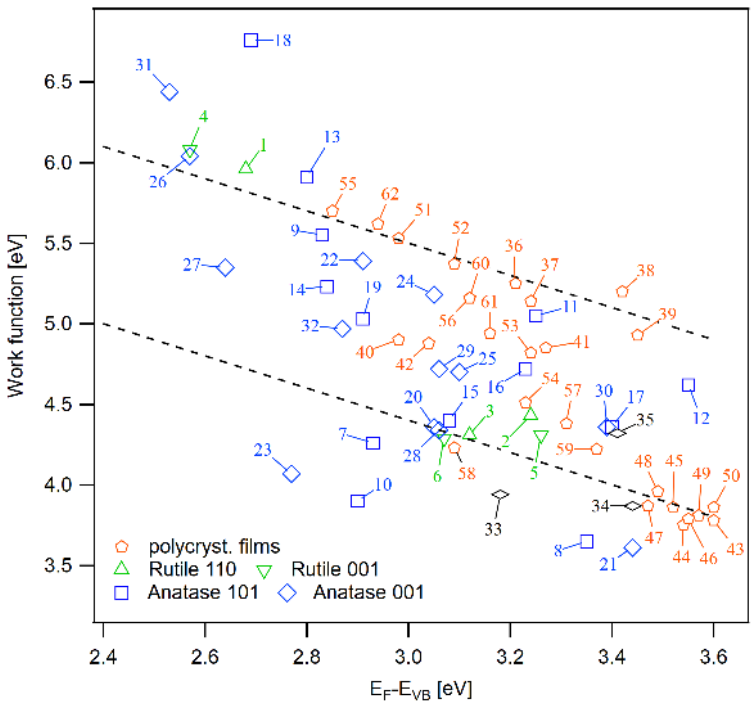

Figure A2. Extended set of work function and Fermi energy data. The description of the sample numbers are given in Table A1.

Table A1. Sample descriptions and surface potentials for Figure A2. All values are in eV with a typical uncertainty of ±0.1 eV.

No.	Sample	Description	E_F	φ	I_P
1	rutile (110)	(i) same as #2; (ii) O_2 plasma, RT, 15 min	2.68	5.96	8.64
2	rutile (110)	(i) 500 °C, 0.5 Pa O_2, 2h; (ii) 600 °C, 10^{-6} Pa, 1 h	3.24	4.43	7.67
3	rutile (110)	same as #2	3.12	4.31	7.43
4	rutile (001)	same as #1	2.57	6.08	8.65
5	rutile (001)	same as #2	3.26	4.31	7.57
6	rutile (001)	same as #2	3.07	4.29	7.36
7	anatase (101)	same as #2	2.93	4.26	7.19
8	anatase (101)	same as #2 + air exposure	3.35	3.65	7.00
9	anatase (101)	O_2 plasma, RT, 15 min	2.83	5.55	8.38
10	anatase (101)	same as #9 + air exposure	2.90	3.90	6.80
11	anatase (101)	(i) same as #12; (ii) O_2 plasma, RT, 15 min; (iii) annealing in 10^{-6} Pa, 200 °C, 20 min	3.25	5.05	8.30
12	anatase (101)	cycles of sputtering + annealing 600 °C, 10^{-6} Pa, 1 h	3.55	4.62	8.17
13	anatase (101)	(i) same as #12; (ii) O_2 plasma, RT, 15 min	2.80	5.91	8.71
14	anatase (101)	stoichiometric as in manuscript	2.84	5.23	8.07
15	anatase (101)	(i) same as #14; (ii) H_2O adsorption	3.08	4.40	7.48
16	anatase (101)	reduced as in manuscript	3.23	4.72	7.95
17	anatase (101)	(i) same #16; (ii) H_2O adsorption	3.4	4.36	7.76
18	anatase (101)	oxidized as in manuscript	2.69	6.76	9.45
19	anatase (101)	(i) same as #18; (ii) H_2O adsorption	2.91	5.03	7.94
20	anatase (001)	same as #7	3.05	4.36	7.41
21	anatase (001)	same as #8	3.44	3.61	7.05
22	anatase (001)	same as #9	2.83	5.55	8.38
23	anatase (001)	same as #10	2.90	3.90	6.80
24	anatase (001)	same as #11	3.25	5.05	8.30
25	anatase (001)	same as #12	3.55	4.62	8.17
26	anatase (001)	same as #13	2.80	5.91	8.71
27	anatase (001)	same as #14	2.84	5.23	8.07
28	anatase (001)	same as #15	3.08	4.4	7.48
29	anatase (001)	same as #16	3.23	4.72	7.95
30	anatase (001)	same as #17	3.40	4.36	7.76
31	anatase (001)	same as #18	2.69	6.76	9.45
32	anatase (001)	same as #19	2.91	5.03	7.94
33	powder	sol-gel, as prepared	3.18	3.94	7.12
34	powder	hydrothermal, as prepared	3.44	3.87	7.31
35	nanocrystals	(101) facetted	3.41	4.32	7.73
36	sprayed film	0.5 Pa O_2, 400 °C, 12 h	3.21	5.25	8.46
37	sprayed film	0.5 Pa Ar, 400 °C, 12 h	3.24	5.14	8.38
38–42	sprayed film	same as #36	2.98–3.45	4.85–5.25	7.88–8.62
43–50	sprayed film	as received	3.47–3.60	3.75–3.96	7.29–7.46
51	thin film	(i) in situ magnetron sputtering at RT; (ii) 0.5 Pa O_2, 600 °C, 1 h	2.98	5.53	8.51
52	thin film	(i) in situ magnetron sputtering at RT; (ii) 0.5 Pa O_2, 400 °C, 1 h	3.09	5.37	8.46
53	sprayed film	same as #11	3.24	4.82	8.06
54	sprayed film	same as #12	3.23	4.51	7.74
55	sprayed film	same as #13	2.85	5.70	8.55
56	sprayed film	stoichiometric as in manuscript	3.12	5.16	8.28
57	sprayed film	(i) same as #58; (ii) H_2O adsorption	3.31	4.23	7.32
58	sprayed film	reduced as in manuscript	3.09	4.23	7.32
59	sprayed film	(i) same as #60; (ii) H_2O adsorption	3.37	4.22	7.59
60	sprayed film	stoichiometric as in manuscript	3.12	5.16	8.28
61	sprayed film	(i) same as #62; (ii) H_2O adsorption	3.16	4.94	8.10
62	sprayed film	oxidized as in manuscript	2.94	5.62	8.56

References

1. Linsebigler, A.L.; Lu, G.; Yates, J.T. Photocatalysis on TiO_2 Surfaces: Principles, Mechanisms, and Selected Results. *Chem. Rev.* **1995**, *95*, 735–758. [CrossRef]
2. Grätzel, M. Solar Energy Conversion by Dye-Sensitized Photovoltaic Cells. *Inorg. Chem.* **2005**, *44*, 6841–6851. [CrossRef] [PubMed]
3. Selcuk, S.; Selloni, A. Facet-dependent trapping and dynamics of excess electrons at anatase TiO_2 surfaces and aqueous interfaces. *Nat. Mater.* **2016**, *15*, 1107. [CrossRef] [PubMed]
4. Diebold, U. The surface science of titanium dioxide. *Surf. Sci. Rep.* **2003**, *48*, 53–229. [CrossRef]
5. Herman, G.S.; Gao, Y. Growth of epitaxial anatase (001) and (101) films. *Thin Solid Films* **2001**, *397*, 157–161. [CrossRef]
6. Setvin, M.; Daniel, B.; Mansfeldova, V.; Kavan, L.; Scheiber, P.; Fidler, M.; Schmid, M.; Diebold, U. Surface preparation of TiO_2 anatase (101): Pitfalls and how to avoid them. *Surf. Sci.* **2014**, *626*, 61–67. [CrossRef]
7. Yang, H.G.; Sun, C.H.; Qiao, S.Z.; Zou, J.; Liu, G.; Smith, S.C.; Cheng, H.M.; Lu, G.Q. Anatase TiO_2 single crystals with a large percentage of reactive facets. *Nature* **2008**, *453*, 638. [CrossRef] [PubMed]
8. Chen, W.; Kuang, Q.; Wang, Q.; Xie, Z. Engineering a high energy surface of anatase TiO_2 crystals towards enhanced performance for energy conversion and environmental applications. *RSC Adv.* **2015**, *5*, 20396–20409. [CrossRef]
9. Liu, G.; Yu, J.C.; Lu, G.Q.M.; Cheng, H.M. Crystal facet engineering of semiconductor photocatalysts: motivations, advances and unique properties. *Chem. Commun.* **2011**, *47*, 6763–6783. [CrossRef] [PubMed]
10. Scheiber, P.; Fidler, M.; Dulub, O.; Schmid, M.; Diebold, U.; Hou, W.; Aschauer, U.; Selloni, A. (Sub)Surface Mobility of Oxygen Vacancies at the TiO_2 Anatase (101) Surface. *Phys. Rev. Lett.* **2012**, *109*, 136103. [CrossRef] [PubMed]
11. Reckers, P.; Dimamay, M.; Klett, J.; Trost, S.; Zilberberg, K.; Riedl, T.; Parkinson, B.A.; Brötz, J.; Jaegermann, W.; Mayer, T. Deep and Shallow TiO_2 Gap States on Cleaved Anatase Single Crystal (101) Surfaces, Nanocrystalline Anatase Films, and ALD Titania Ante and Post Annealing. *J. Phys. Chem. C* **2015**, *119*, 9890–9898. [CrossRef]
12. Baldini, E.; Chiodo, L.; Dominguez, A.; Palummo, M.; Moser, S.; Yazdi-Rizi, M.; Auböck, G.; Mallett, B.P.; Berger, H.; Magrez, A. Strongly bound excitons in anatase TiO_2 single crystals and nanoparticles. *Nat. Commun.* **2017**, *8*, 13. [CrossRef] [PubMed]
13. Moser, S.; Moreschini, L.; Jaćimović, J.; Barišić, O.S.; Berger, H.; Magrez, A.; Chang, Y.J.; Kim, K.S.; Bostwick, A.; Rotenberg, E.; et al. Tunable Polaronic Conduction in Anatase TiO_2. *Phys. Rev. Lett.* **2013**, *110*, 196403. [CrossRef] [PubMed]
14. Emori, M.; Sakino, A.; Ozawa, K.; Sakama, H. Polarization-dependent ARPES measurement for valence band of anatase TiO_2. *Solid State Commun.* **2014**, *188*, 15–18. [CrossRef]
15. Sandell, A.; Sanyal, B.; Walle, L.; Richter, J.; Plogmaker, S.; Karlsson, P.; Borg, A.; Uvdal, P. Probing and modifying the empty-state threshold of anatase TiO_2: Experiments and ab initio theory. *Phys. Rev. B* **2008**, *78*, 075113. [CrossRef]
16. Tuan, A.C.; Kaspar, T.C.; Droubay, T.; Rogers , J.W., Jr.; Chambers, S.A. Band offsets for the epitaxial $TiO_2/SrTiO_3/Si(001)$ system. *Appl. Phys. Lett.* **2003**, *83*, 3734–3736. [CrossRef]
17. Thomas, A.G.; Flavell, W.R.; Kumarasinghe, A.R.; Mallick, A.K.; Tsoutsou, D.; Smith, G.C.; Stockbauer, R.; Patel, S.; Grätzel, M.; Hengerer, R. Resonant photoemission of anatase TiO_2 (101) and (001) single crystals. *Phys. Rev. B* **2003**, *67*, 035110. [CrossRef]
18. Thomas, A.G.; Flavell, W.R.; Mallick, A.K.; Kumarasinghe, A.R.; Tsoutsou, D.; Khan, N.; Chatwin, C.; Rayner, S.; Smith, G.C.; Stockbauer, R.L.; et al. Comparison of the electronic structure of anatase and rutile TiO_2 single-crystal surfaces using resonant photoemission and X-ray absorption spectroscopy. *Phys. Rev. B* **2007**, *75*, 035105. [CrossRef]
19. Pfeifer, V.; Erhart, P.; Li, S.; Rachut, K.; Morasch, J.; Brötz, J.; Reckers, P.; Mayer, T.; Rühle, S.; Zaban, A.; et al. Energy Band Alignment Between Anatase and Rutile TiO_2. *J. Phys. Chem. Lett.* **2013**, *4*, 4182–4187. [CrossRef]
20. Schwanitz, K.; Weiler, U.; Hunger, R.; Mayer, T.; Jaegermann, W. Synchrotron-induced photoelectron spectroscopy of the dye-sensitized nanocrystalline TiO_2/electrolyte interface: Band gap states and their interaction with dye and solvent molecules. *J. Phys. Chem. C* **2007**, *111*, 849–854. [CrossRef]

21. Liu, G.; Schulmeyer, T.; Thissen, A.; Klein, A.; Jaegermann, W. In situ preparation and interface characterization of TiO_2/Cu_2S heterointerface. *Appl. Phys. Lett.* **2003**, *82*, 2269–2271. [CrossRef]
22. Henrich, V.E.; Dresselhaus, G.; Zeiger, H.J. Observation of Two-Dimensional Phases Associated with Defect States on the Surface of TiO_2. *Phys. Rev. Lett.* **1976**, *36*, 1335–1339. [CrossRef]
23. Thompson, T.L.; Diwald, O.; Yates, J.T. CO_2 as a Probe for Monitoring the Surface Defects on TiO_2(110)Temperature-Programmed Desorption. *J. Phys. Chem. B* **2003**, *107*, 11700–11704. [CrossRef]
24. Borodin, A.; Reichling, M. Characterizing TiO_2(110) surface states by their work function. *Phys. Chem. Chem. Phys.* **2011**, *13*, 15442–15447. [CrossRef] [PubMed]
25. Klein, A.; Körber, C.; Wachau, A.; Säuberlich, F.; Gassenbauer, Y.; Schafranek, R.; Harvey, S.P.; Mason, T.O. Surface Potentials of Magnetron Sputtered Transparent Conducting Oxides. *Thin Solid Films* **2009**, *518*, 1197–1203. [CrossRef]
26. Goniakowski, J.; Finocchi, F.; Noguera, C. Polarity of oxide surfaces and nanostructures. *Rep. Prog. Phys.* **2008**, *71*, 016501. [CrossRef]
27. Ishii, H.; Sugiyama, K.; Ito, E.; Seki, K. Energy Level Alignment and Interfacial Electronic Structures at Organic/Metal and Organic/Organic Interfaces. *Adv. Mater.* **1999**, *11*, 605–625. [CrossRef]
28. Batzill, M.; Diebold, U. The surface and materials science of tin oxide. *Prog. Surf. Sci.* **2005**, *79*, 47–154. [CrossRef]
29. Klein, A.; Körber, C.; Wachau, A.; Säuberlich, F.; Gassenbauer, Y.; Harvey, S.P.; Proffit, D.E.; Mason, T.O. Transparent Conducting Oxides for Photovoltaics: Manipulation of Fermi Level, Work Function, and Energy Band Alignment. *Materials* **2010**, *3*, 4892–4914. [CrossRef] [PubMed]
30. Hohmann, M.V.; Ágoston, P.; Wachau, A.; Bayer, T.J.M.; Brötz, J.; Albe, K.; Klein, A. Orientation Dependent Ionization Potential of In_2O_3: A Natural Source for Inhomogeneous Barrier Formation at Electrode Interfaces in Organic Electronics. *J. Phys. Condens. Matter* **2011**, *23*, 334203. [CrossRef] [PubMed]
31. Wardenga, H.; Klein, A. Surface Potentials of (111), (110) and (100) oriented CeO_{2-x} thin films. *Appl. Surf. Sci.* **2016**, *377*, 1–8. [CrossRef]
32. Morgan, B.J.; Watson, G.W. A Density Functional Theory + U Study of Oxygen Vacancy Formation at the (110), (100), (101), and (001) Surfaces of Rutile TiO_2. *J. Phys. Chem. C* **2009**, *113*, 7322–7328. [CrossRef]
33. Cheng, H.; Selloni, A. Surface and subsurface oxygen vacancies in anatase TiO_2 and differences with rutile. *Phys. Rev. B* **2009**, *79*, 092101. [CrossRef]
34. Li, H.; Guo, Y.; Robertson, J. Calculation of TiO_2 Surface and Subsurface Oxygen Vacancy by the Screened Exchange Functional. *J. Phys. Chem. C* **2015**, *119*, 18160–18166. [CrossRef]
35. He, Y.; Dulub, O.; Cheng, H.; Selloni, A.; Diebold, U. Evidence for the Predominance of Subsurface Defects on Reduced Anatase $TiO_2(101)$. *Phys. Rev. Lett.* **2009**, *102*, 106105. [CrossRef] [PubMed]
36. Bahnemann, D. Photocatalytic water treatment: solar energy applications. *Solar Energy* **2004**, *77*, 445–459. [CrossRef]
37. Fujishima, A.; Zhang, X.; Tryk, D.A. TiO_2 photocatalysis and related surface phenomena. *Surf. Sci. Rep.* **2008**, *63*, 515–582. [CrossRef]
38. De Angelis, F.; Valentin, C.D.; Fantacci, S.; Vittadini, A.; Selloni, A. Theoretical Studies on Anatase and Less Common TiO_2 Phases: Bulk, Surfaces, and Nanomaterials. *Chem. Rev.* **2014**, *114*, 9708–9753. [CrossRef] [PubMed]
39. Bourikas, K.; Kordulis, C.; Lycourghiotis, A. Titanium Dioxide (Anatase and Rutile): Surface Chemistry, Liquid-Solid Interface Chemistry, and Scientific Synthesis of Supported Catalysts. *Chem. Rev.* **2014**, *114*, 9754–9823. [CrossRef] [PubMed]
40. Pang, C.L.; Lindsay, R.; Thornton, G. Chemical reactions on rutile TiO_2(110). *Chem. Soc. Rev.* **2008**, *37*, 2328–2353. [CrossRef] [PubMed]
41. Hussain, H.; Tocci, G.; Woolcot, T.; Torrelles, X.; Pang, C.L.; Humphrey, D.S.; Yim, C.M.; Grinter, D.C.; Cabailh, G.; Bikondoa, O.; et al. Structure of a model TiO_2 photocatalytic interface. *Nat. Mater.* **2017**, *16*, 461. [CrossRef] [PubMed]
42. Vittadini, A.; Selloni, A.; Rotzinger, F.P.; Grätzel, M. Structure and Energetics of Water Adsorbed at TiO_2 Anatase (101) and (001) Surfaces. *Phys. Rev. Lett.* **1998**, *81*, 2954–2957. [CrossRef]
43. Aschauer, U.; He, Y.; Cheng, H.; Li, S.C.; Diebold, U.; Selloni, A. Influence of Subsurface Defects on the Surface Reactivity of TiO_2: Water on Anatase (101). *J. Phys. Chem. C* **2010**, *114*, 1278–1284. [CrossRef]

44. Li, Y.; Gao, Y. Interplay between Water and TiO_2 Anatase (101) Surface with Subsurface Oxygen Vacancy. *Phys. Rev. Lett.* **2014**, *112*, 206101. [CrossRef]
45. Jackman, M.J.; Thomas, A.G.; Muryn, C. Photoelectron Spectroscopy Study of Stoichiometric and Reduced Anatase TiO_2(101) Surfaces: The Effect of Subsurface Defects on Water Adsorption at Near-Ambient Pressures. *J. Phys. Chem. C* **2015**, *119*, 13682–13690. [CrossRef]
46. Liu, L.; Zhao, H.; Andino, J.M.; Li, Y. Photocatalytic CO_2 Reduction with H_2O on TiO_2 Nanocrystals: Comparison of Anatase, Rutile, and Brookite Polymorphs and Exploration of Surface Chemistry. *ACS Catal.* **2012**, *2*, 1817–1828. [CrossRef]
47. Duncan, D.; Allegretti, F.; Woodruff, D. Water does partially dissociate on the perfect TiO_2 (110) surface: A quantitative structure determination. *Phys. Rev. B* **2012**, *86*, 045411. [CrossRef]
48. Walle, L.E.; Borg, A.; Uvdal, P.; Sandell, A. Experimental evidence for mixed dissociative and molecular adsorption of water on a rutile TiO_2 (110) surface without oxygen vacancies. *Phys. Rev. B* **2009**, *80*, 235436. [CrossRef]
49. Mu, R.; Zhao, Z.J.; Dohnálek, Z.; Gong, J. Structural motifs of water on metal oxide surfaces. *Chem. Soc. Rev.* **2017**, *46*, 1785–1806. [CrossRef] [PubMed]
50. Patrick, C.E.; Giustino, F. Structure of a water monolayer on the anatase TiO_2 (101) surface. *Phys. Rev. Appl.* **2014**, *2*, 014001. [CrossRef]
51. Henrion, O.; Klein, A.; Pettenkofer, C.; Jaegermann, W. Low temperature adsorption of water on cleaved GaAs(110) surfaces. *Surf. Sci. Lett.* **1996**, *366*, L685. [CrossRef]
52. Klein, A. Interface Properties of Dielectric Oxides. *J. Am. Ceram. Soc.* **2016**, *99*, 369–387. [CrossRef]
53. Wendt, S.; Sprunger, P.T.; Lira, E.; Madsen, G.K.H.; Li, Z.; Hansen, J.O.; Matthiesen, J.; Blekinge-Rasmussen, A.; Lægsgaard, E.; Hammer, B.; et al. The Role of Interstitial Sites in the Ti3d Defect State in the Band Gap of Titania. *Science* **2008**, *320*, 1755–1759. [CrossRef] [PubMed]
54. Li, M.; Hebenstreit, W.; Gross, L.; Diebold, U.; Henderson, M.A.; Jennison, D.R.; Schultz, P.A.; Sears, M.P. Oxygen-induced restructuring of the TiO_2(110) surface: A comprehensive study. *Surf. Sci.* **1999**, *437*, 173–190. [CrossRef]
55. Wu, C.C.; Wu, C.I.; Sturm, J.C.; Kahn, A. Surface modification of indium tin oxide by plasma treatment: An effective method to improve the efficiency, brightness, and reliability of organic light emitting devices. *Appl. Phys. Lett.* **1997**, *70*, 1348. [CrossRef]
56. Klissurski, D.; Hadjiivanov, K.; Kantcheva, M.; Gyurova, L. Study of peroxide-modified titanium dioxide (anatase). *J. Chem. Soc. Faraday Trans.* **1990**, *86*, 385–388. [CrossRef]
57. Iwamoto, M.; Yoda, Y.; Yamazoe, N.; Seiyama, T. Study of metal oxide catalysts by temperature programmed desorption. 4. Oxygen adsorption on various metal oxides. *J. Phys. Chem.* **1978**, *82*, 2564–2570. [CrossRef]
58. Bayer, T.J.M.; Wachau, A.; Fuchs, A.; Deuermeier, J.; Klein, A. Atomic layer deposition of Al_2O_3 onto Sn-doped In_2O_3: Absence of self-limited adsorption during initial growth by oxygen diffusion from the substrate and band offset modification by Fermi level pinning in Al_2O_3. *Chem. Mater.* **2012**, *24*, 4503–4510. [CrossRef]
59. Klein, A. Transparent Conducting Oxides: Electronic Structure - Property Relationship from Photoelectron Spectroscopy with in-situ Sample Preparation. *J. Am. Ceram. Soc.* **2013**, *96*, 331–345. [CrossRef]
60. Idriss, H.; Barteau, M.A. Characterization of TiO_2 surfaces active for novel organic syntheses. *Catal. Lett.* **1994**, *26*, 123–139. [CrossRef]
61. Moulder, J.F.; Stickle, W.F.; Sobol, P.E.; Bomben, K.D. *Handbook of X-ray Photoelectron Spectroscopy*; Physical Electronics, Inc.: Eden Prairie, MN, USA, 1995.
62. Yesodharan, E.; Grätzel, M. Photodecomposition of Liquid Water with TiO_2? Supported Noble Metal Clusters. *Helv. Chim. Acta* **1983**, *66*, 2145–2153. [CrossRef]
63. Kodaira, S.; Sakisaka, Y.; Maruyama, T.; Haruyama, Y.; Aiura, Y.; Kato, H. Angle-resolved photoemission study of an in-gap state in TiO_2. *Solid State Commun.* **1994**, *89*, 9–12. [CrossRef]
64. Finazzi, E.; Valentin, C.D.; Pacchioni, G.; Selloni, A. Excess electron states in reduced bulk anatase TiO_2: Comparison of standard GGA, GGA+U, and hybrid DFT calculations. *J. Chem. Phys.* **2008**, *129*, 154113. [CrossRef] [PubMed]
65. Ohno, T.; Sarukawa, K.; Matsumura, M. Crystal faces of rutile and anatase TiO_2 particles and their roles in photocatalytic reactions. *New J. Chem.* **2002**, *26*, 1167–1170. [CrossRef]

66. Yu, J.; Low, J.; Xiao, W.; Zhou, P.; Jaroniec, M. Enhanced Photocatalytic CO_2-Reduction Activity of Anatase TiO_2 by Coexposed 001 and 101 Facets. *J. Am. Chem. Soc.* **2014**, *136*, 8839–8842. [CrossRef] [PubMed]
67. Dette, C.; Pérez-Osorio, M.A.; Kley, C.S.; Punke, P.; Patrick, C.E.; Jacobson, P.; Giustino, F.; Jung, S.J.; Kern, K. TiO_2 Anatase with a Bandgap in the Visible Region. *Nano Lett.* **2014**, *14*, 6533–6538. [CrossRef] [PubMed]
68. King, P.D.C.; Veal, T.D.; Fuchs, F.; Wang, C.Y.; Payne, D.J.; Bourlange, A.; Zhang, H.; Bell, G.R.; Cimalla, V.; Ambacher, O.; et al. Band gap, electronic structure, and surface electron accumulation of cubic and rhombohedral In_2O_3. *Phys. Rev. B* **2009**, *79*, 205211. [CrossRef]
69. Berthold, T.; Rombach, J.; Stauden, T.; Polyakov, V.; Cimalla, V.; Krischok, S.; Bierwagen, O.; Himmerlich, M. Consequences of plasma oxidation and vacuum annealing on the chemical properties and electron accumulation of In_2O_3 surfaces. *J. Appl. Phys.* **2016**, *120*, 245301. [CrossRef]
70. Vasheghani Farahani, S.K.; Veal, T.D.; Mudd, J.J.; Scanlon, D.O.; Watson, G.W.; Bierwagen, O.; White, M.E.; Speck, J.S.; McConville, C.F. Valence-band density of states and surface electron accumulation in epitaxial SnO_2 films. *Phys. Rev. B* **2014**, *90*, 155413. [CrossRef]
71. Körber, C.; Ágoston, P.; Klein, A. Surface and Bulk Properties of Sputter Deposited Intrinsic and Doped SnO_2 Thin Films. *Sens. Actuators B* **2009**, *139*, 665–672. [CrossRef]
72. Rachut, K.; Körber, C.; Brötz, J.; Klein, A. Growth and Surface Properties of Epitaxial SnO_2. *Phys. Stat. Sol. (A)* **2014**, *211*, 1997–2004. [CrossRef]
73. Batzill, M.; Katsiev, K.; Burst, J.M.; Diebold, U.; Chaka, A.M.; Delley, B. Gas-phase-dependent properties of SnO_2 (110), (100), and (101) single-crystal surfaces: Structure, composition, and electronic properties. *Phys. Rev. B* **2005**, *72*, 165414. [CrossRef]
74. Cox, D.F.; Fryberger, T.B.; Semancik, S. Oxygen vacancies and defect electronic states on the SnO_2(110)-1×1 surface. *Phys. Rev. B* **1988**, *38*, 2072–2083. [CrossRef]
75. Ágoston, P.; Albe, K. Disordered reconstructions of the reduced SnO_2-(110) surface . *Surf. Sci.* **2011**, *605*, 714–722. [CrossRef]
76. Deák, P.; Aradi, B.; Frauenheim, T. Band Lineup and Charge Carrier Separation in Mixed Rutile-Anatase Systems. *J. Phys. Chem. C* **2011**, *115*, 3443–3446. [CrossRef]
77. Scanlon, D.O.; Dunnill, C.W.; Buckeridge, J.; Shevlin, S.A.; Logsdail, A.J.; Woodley, S.M.; Catlow, C.R.A.; Powell, M.J.; Palgrave, R.G.; Parkin, I.P.; et al. Band alignment of rutile and anatase TiO_2. *Nat. Mater.* **2013**, *12*, 798. [CrossRef] [PubMed]